www.elsevier.com/locate/jmbbm

Ti-6Al-4V triply periodic minimal surface structures for bone implants fabricated via selective laser melting

Chunze Yan, Liang Hao, Ahmed Hussein, Philippe Young

PII: S1751-6161(15)00229-5
DOI: http://dx.doi.org/10.1016/j.jmbbm.2015.06.024
Reference: JMBBM1518

To appear in: *Journal of the Mechanical Behavior of Biomedical Materials*

Cite this article as: Chunze Yan, Liang Hao, Ahmed Hussein, Philippe Young, Ti-6Al-4V triply periodic minimal surface structures for bone implants fabricated via selective laser melting, *Journal of the Mechanical Behavior of Biomedical Materials,* http://dx.doi.org/10.1016/j.jmbbm.2015.06.024

Ti-6Al-4V triply periodic minimal surface structures for bone implants fabricated via selective laser melting

Chunze Yan [a, b, *], Liang Hao [b, *], Ahmed Hussein [b], Philippe Young [b]

[a] *State key Laboratory of Materials Processing and Die & Mould Technology, Huazhong University of Science and Technology. Wuhan 430074, Hubei, China.*

[b] *College of Engineering, Mathematics and Physical Sciences, University of Exeter, Exeter EX4 4QF, Devon, United Kingdom*

Abstract

Triply periodic minimal surface (TPMS) structures have already been shown to be a versatile source of biomorphic scaffold designs. Therefore, in this work, Ti-6Al-4V Gyroid and Diamond TPMS lattices having an interconnected high porosity of 80-95% and pore sizes in the range of 560-1600 μm and 480-1450 μm respectively were manufactured by selective laser melting (SLM) for bone implants. The manufacturability, microstructure and mechanical properties of the Ti-6Al-4V TPMS lattices were evaluated. Comparison between 3D micro-CT reconstructed models and original CAD models of the Ti-6Al-4V TPMS lattices shows excellent reproduction of the designs. The as-built Ti-6Al-4V struts exhibit the microstructure of columnar grains filled with very fine and orthogonally oriented α' martensitic laths with the width of 100~300 nm and have the microhardness of 4.01±0.34 GPa. After heat treatment at 680^{o}C for 4 h, the α' martensite was converted to a mixture of α and β, in which the α phase being the dominant fraction is present as fine laths with the width of 500-800 nm and separated by a small amount of narrow, interphase regions of dark β phase. Also, the microhardness is decreased to 3.71±0.35 GPa due to the coarsening of the microstructure. The 80-95% porosity TPMS lattices exhibit a comparable

porosity with trabecular bone, and the modulus is in the range of 0.12-1.25 GPa and thus can be adjusted to the modulus of trabecular bone. At the same range of porosity of 5-10%, the moduli of cortical bone and of the Ti-6Al-4V TPMS lattices are in a similar range. Therefore, the modulus and porosity of Ti-6Al-4V TPMS lattices can be tailored to the levels of human bones and thus reduce or avoid "stress shielding" and increase longevity of implants. Due to the biomorphic designs, and high interconnected porosity and stiffness comparable to human bones, SLM-made Ti-6Al-4V TPMS lattices can be a promising material for load bearing bone implants.

Keywords: Additive manufacturing; selective laser melting; Titanium alloys; Triply periodic minimal surface; porous materials

* Corresponding authors. Tel: +44(0)1392723665; E-mail address:
l.hao@exeter.ac.uk (L. Hao), c.yan@exeter.ac.uk (C. Yan)

1 Introduction

Pure titanium and some of its alloys have been widely used for long-term and load-bearing bone implants in the orthopaedic and dental fields, due to their good biocompatibility, high strength-to-weight ratio and fatigue resistance, superior corrosion resistance and lower modulus when compared with other metal biomaterials, such as cobalt alloy and stainless steel (Heinl et al., 2008; Fujibayashi et al., 2004). However, solid titanium materials still show much higher moduli than natural bones. For instance, dense Ti6-Al4-V has a Young's modulus of around 110 GPa, considerably greater than those of the natural bones (that of cortical and trabecular bone ranging from 0.5 GPa to a maximum 20 GPa) (Parthasarathy et al., 2010). The huge mismatch of modulus between an implant and the surrounding bones generally

induces uneven stress distribution at the bone-implant interface, leading to bone resorption around metallic implants, increased fracture risks in the weakened bone and loosening of the implants. This phenomenon is referred to as “stress shielding”, which normally reduces the longevity of the implants (Huiskes et al., 1992). Thus, it is very desirable to develop metallic biomaterials for implants with the modulus comparable to those of natural bones.

Natural bones belong to porous materials with interconnected voids, and are comprised of the outer cortical bone and inner trabecular bone. The cortical bone is relatively dense and strong with a porosity ranging from 5% to 10%, whereas trabecular bone is more porous and weaker with a higher porosity of 50-90% (Sikavitsas et al., 2001). Therefore, porous titanium materials possessing similar interconnected pores and porosity with natural bones are of particular interest for orthopaedic and dental implant applications. More importantly, incorporating interconnected pores in titanium implants present a promising method to reduce the moduli to the level of natural bones and thus reduce or avoid “stress shielding” and increase longevity of implants. Moreover, the presence of interconnected pores with an appropriate pore size can provide biological anchorage for the surrounding bony tissue via the ingrowth of mineralized tissue into the pore space (van Blitterswijk et al., 1986).

Nowadays, conventional techniques available for the fabrication of open-cell porous titanium structures mainly include controlled powder sintering (Oh et al., 2003), polymeric sponge relication (Li et al., 2005), molding and sintering of short metal fibres (Galante et al., 1973) and solid-state foaming by expansion of argon-filled pores (Davis et al., 2001). But, these conventional manufacturing techniques do not allow realization of well-defined internal structures with pore interconnectivity

and highly controllable volume fraction, pore geometry, pore size and distribution, and complex external shapes. Selective laser melting (SLM), also termed as direct metal laser sintering (DMLS), and electron beam melting (EBM) are the powder bed fusion (PBF) processes of additive manufacturing (AM) technologies, and capable of fabricating near-fully dense metal components with complex freeform geometries directly from computer-aided design (CAD) models (Koike et al., 2011), therefore showing great potential to fabricate metallic cellular lattice structures beyond the current limitations of the conventional manufacturing techniques. Recently, many attempts have been made to fabricate porous titanium scaffolds or orthopaedic implants with precisely controlled internal structures and complex external shapes through SLM or EBM (Mullen et al., 2009; Bertol et al., 2010; Gorny et al., 2011; Murr et al., 2010; Heinl et al., 2008; Parthasarathy et al., 2010; Sallica-Leva et al., 2013). For example, Mullen et al. (2009) built cellular titanium structures based on an octahedral unit cell through SLM for orthopaedic applications, and the produced structures possessed the porosity of 10-95% and compressive strength of 0.5-350MPa comparable to the typical naturally occurring range of natural bones. Parthasarathy et al., (2010) fabricated porous titanium structures with fully interconnected porosities varying from 49.75%-70.32% by EBM. However, majority of existing titanium scaffolds made by SLM and EBM are based on cubic lattices with straight edges and sharp turns or those derived from Boolean intersections of geometric primitives such as spheres and cylinders. Neither of these partitions provides a biomorphic environment suitable for cell attachment, migration and proliferation (Rajagopalan et al., 2006, Spalazzi et al., 2003), because the aggregates of cells in foam/extracellular matrix naturally have cells separated by curved partitions (Yousaf, et al., 2001). Moreover, these cellular with sharp turning and straight edged pores and struts would

not exhibit good manufacturability in SLM and EBM in large unit cell sizes and low volume fractions as resultant long overhangs will lead to thermal deformation (Yan et al., 2011).

The biomorphic geometry that best mimics the secundam-naturam substrate would be surfaces that are continuous through space and divided into two not-necessarily-equal sub-spaces by a nonintersecting two-sided surface (Rajagopalan et al., 2006). Triply periodic minimal surface (TPMS) structures are smooth infinite surfaces that partition the space into two labyrinths in the absence of self-intersections, and are periodic in three independent directions (Kapfer et al., 2011). TPMS structures are ideal to describe the above-mentioned biomorphic space. Due to the high structural complexity of TPMS, currently only AM technologies realize the fabrication of mathematically defined TPMS engineering scaffold architectures using polymers. Rajagopalan et al. (2006) physically realized the Schwarz Primitive TPMS through a combined process of AM and injection molding mainly including the AM manufacturing of a wax mold and then injection of poly(propylene fumarate). They justified the natural affinity of the TPMS structures in biological forms and biological sciences, and provided sufficient evidence for their suitability as viable tissue analogues. Melchels et al. (2010a) fabricated the scaffold architectures based on Diamond and Gyroid TPMS for tissue engineering by the Stereolithography (SLA) AM technology using the materials of poly(D, L-lactide) and poly(D, L-lactide-co-ε-caprolactone). Melchels et al. (2010b) investigated the effect of scaffold pore architecture on cell seeding and static culturing, by comparing a Gyroid TPMS architecture fabricated by SLA with a random pore architecture. Although both scaffold types showed comparable porosity and pore size values, the gyroid TPMS type showed a more than 10-fold higher permeability due to the absence of size-

limiting pore interconnections. In the previous literature, the modulation of porosity, pose size and mechanical properties, the viability of cells on TMPS cellular structures, and TMPS-philicity of biological systems have presented compelling evidence to propose TMPS-based scaffolds as viable orthopaedic tissue analogues (Rajagopalan et al., 2006).

Although TPMS have already been shown to be a more versatile source of biomorphic scaffold designs than currently reported in the tissue engineering literature (Kapfer et al., 2011), to the best of our knowledge, no published work has been carried out to investigate the manufacturability and properties of titanium alloy TPMS structures for tissue engineering or orthopaedic implants fabricated by SLM. Therefore, in this work, Ti-6Al-4V Gyroid and Diamond TPMS lattices having an interconnected high porosity ranging of 80-95% and pore sizes in the range of 560-1600 μm and 480-1450 μm respectively were manufactured by SLM for bone implants. The manufacturability, microstructure and mechanical properties of the Ti-6Al-4V TPMS lattices were investigated.

2 Experimental

2.1. Materials

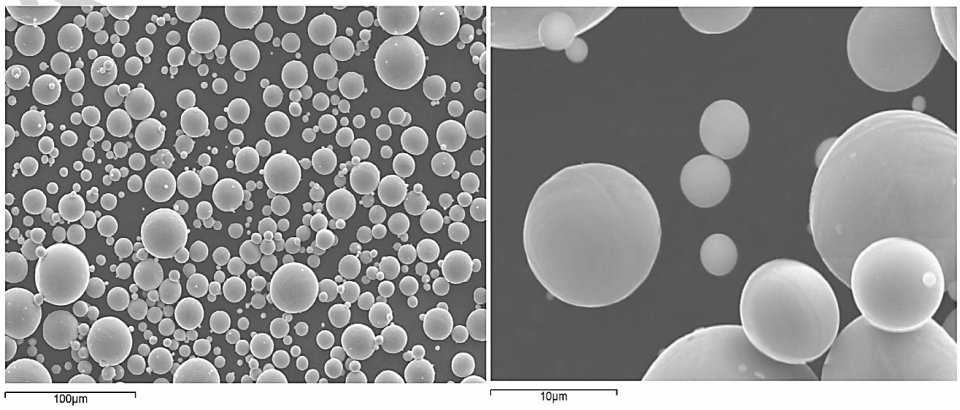

Figure 1 SEM images of the Ti-6Al-4V powder with different magnifications

The Ti-6Al-4V powder was bought from Electro Optical System (EOS) GmbH, Germany. Fig. 1 shows the SEM images of the as-received alloy powder at different magnifications. The powder particles exhibit a nearly spherical shape and smooth surfaces, indicating a good flowability. The powder shows a particle size distribution of 3-50 μm and average particle size of about 20 μm.

2.2. Design and SLM manufacturing process of TPMS structures

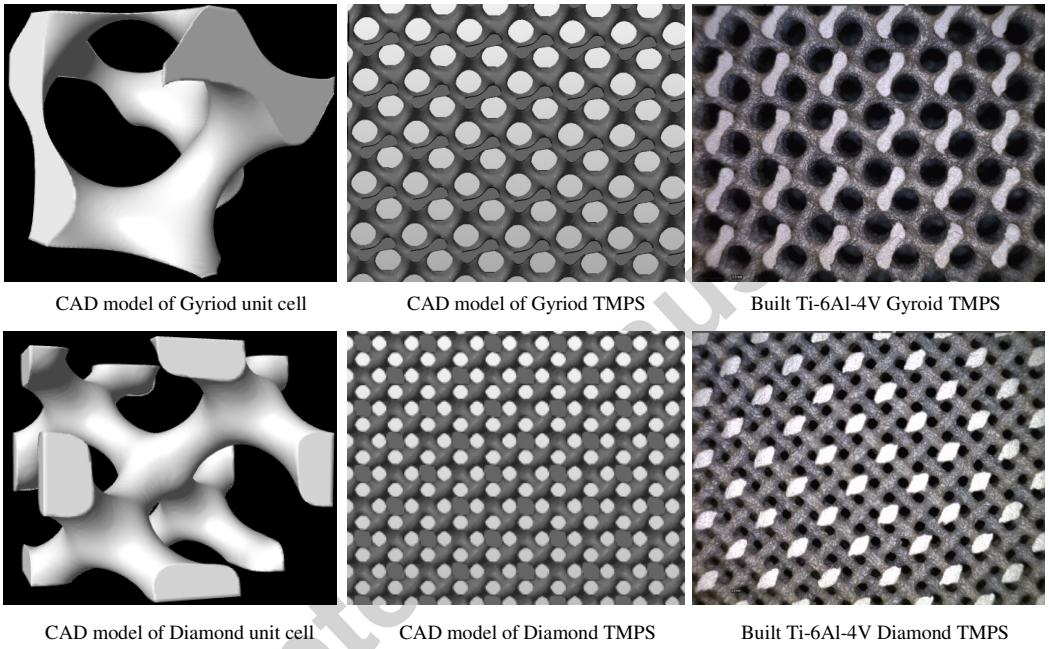

Figure 2 CAD models of the unit cells and TMPS cellular structures, and optical micrographs of SLM-made Ti-6Al-4V TMPS cellular structures

The Diamond minimal surface discovered by Schwarz (1885) and Gyroid minimal surface discovered by Schoen (1970) both belong to TMPS. The Gyroid and Diamond unit cells are mathematically defined by a computational method that allows precise control of volume fraction and unit cell size, which is reported in our previous work (Hao et al., 2011). The Gyroid and Diamond TMPS cellular structures were constructed by repeating the gyroid and Diamond unit cells, respectively. The CAD models of Gyroid and Diamond unit cells and their TMPS cellular structures were

generated using the $^{+}$CAD software developed by Simpleware Ltd. UK, as shown in Fig. 2.

The TPMS cellular samples with the volume fractions of 5%, 7.5%, 10%, 12.5%, 15% and 20% were fabricated by 3T RPD Ltd. UK using DMLS EOSINT-M270 machine supplied by EOS GmbH, Munich, Germany. For each volume fraction, the TMPS cellular structures with the unit cell sizes of 3mm, 3.5mm, 4mm, 4.5mm, 5mm, 5.5mm, 6mm, 6.5mm and 7mm were manufactured. The used processing parameters that have been optimized for the Ti-6Al-4V powder are: the laser power of 170 W, the scanning speed of 1250 mm/s, the spot size of 100 µm, the < 0.1 % oxygen content, the layer thickness of 30µm and the hatch spacing of 60 µm. The scanning strategy was associated to an alternating hatch pattern, where the direction of scanning was rotated of 67^{o} between consecutive layers. The as-built samples were subjected to a post processing including a thermal stress-relieving heat treatment cycle (heat treated at 680 ^{o}C for 4 h and then cooled down in the furnace to RT) in an argon atmosphere, followed by ceramic bead blasting. Finally, the Ti-6Al-4V TMPS cellular structures were obtained by the removal from the base plate via wire Electrical Discharge Machining (wire-EDM). The optical micrographs of the Ti-6Al-4V TMPS cellular structures were also shown in Fig. 2.

2.4. Measurements and characterisations

Uni-axial compression tests were carried out at a loading rate of 0.4 mm/min using an EZ20 Universal Material Testing Machine, Lloyd Instruments Ltd., UK. For each data point, four samples were tested and the average value was taken. For microstructure analysis, the struts of the cellular structures were cross-sectioned, and then polished down to colloidal silica suspension and etched with using Kroll's reagent (containing 100 mL water, 2.5 mL hydrogen fluoride and 5.0 mL nitric acid)

for 30 s. The microstructure was observed by an optical microscopy (4XCE, Caikon), scanning electron microscopy (SEM, JEOL JSM-6390LV) and transmission electron microscopy (TEM, JEOL 1400, operated at 200 kV). For TEM sample preparation, 3mm diameter samples were punched from thin sheets with 0.3mm thickness and ground to approximately 0.04mm thickness. A Model 1020 Argon Ion Milling was used to produce thin foils. The struts of the lattice structures mounted in resin were polished down to 1 μm colloidal silica suspension for the Vickers micro-hardness measurements by using Future-Tech Microhardness Tester FM with the 500gf load for a 10s dwell time, where the indenter was placed within a single strut at least 3 imprint diameters away from its edges. Six measurements were done to calculate a mean hardness value. X-ray diffraction (XRD) measurement was conducted with a Bruker D8 Advanced X-ray diffractometer, with CuKa radiation (wavelength λ=0.154 nm), a step size of 0.02^{o}, and a time step of two seconds for normal scan, over a 2θ range of 20-80^{o}. A micro-computer tomography (CT) scanner (Benchtop CT 160Xi, X-Tek) with a 27μm resolution was used to scan the lattice structures at 120KV voltage and 182μA current, and two-dimensional (2D) slice image data were collected. VGstudio MAX2.1 software reconstructed the 3D models of the fabricated cellular lattice structures through the 2D slice images data obtained from micro-CT scans. The strut density of the lattice structures was measured by comparing the weight in water and air, according to the Archimedes' principle. The relative densities were expressed in % by the ratio of the strut density to Ti-6Al-4V theoretical bulk density, 4.43 g/cm^3.

3 Results and discussion

3.1 Analysis of built structures

Figure 3 shows the SEM morphologies of strut surface of the as-built Ti-6Al-4V TMPS cellular structure without post processing. It can be observed that there are many small spherical particles visible on the surface. The size and morphology of the particles are very similar to those of the Ti-6Al-4V powder as shown in Fig. 2. The bonded metal particles on surfaces of the lattice struts may be explained by the following reasons: (1) The curved struts with varying inclined angles were partially built on the loose powder, and thus some metal particles below each layer were totally or partially melted and then bonded on the bottom of the layer . (2) Thermal diffusion occured between loose powder and solidified material due to big temperature difference, leading to powder particles sticking to the strut surface (Van Bael et al., 2011). (3) Some metal particles on the boundary are partially melted by the contour laser track, and then bonded to the boundary of each layer (Yan et al., 2011). These bonded partilces can be deleterious to the mechanical properties, especially fatigue strength (Hrabe et al., 2011). Moreover, they are partially bonded to the strut surfaces, and may, therefore, be released to the biological systems, resulting in inflammation (Sallica-Leva et al., 2013).

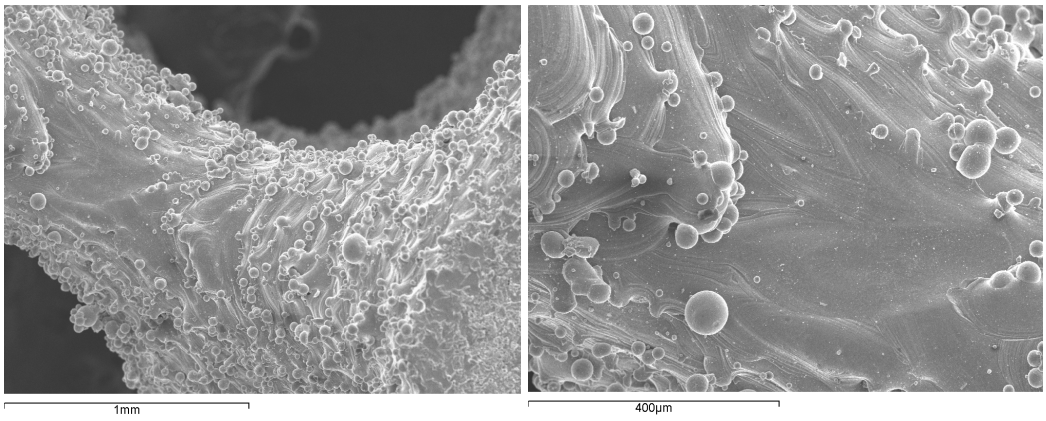

Figure 3 SEM images of strut surface of the as-built Ti-6Al-4V TMPS cellular structures without post processing

In order to remove the bonded metal particals and improve the surface quality of the struts, the as-built cellular structures were subjected to a post processing of heat treatment followed by sand blasting. Fig. 4 shows the SEM images of the strut surfaces of the Ti-6Al-4V TMPS cellular structures after the post processing. It can be seen that nearly all the bonded particles are removed, and the strut surfaces become smoother compared to the original surfaces before the post processing as shown in Fig. 3 although there still exit the corrugations. The heat treatment may make partially melted metal particles fused and bonded with the laser melted core parts of the struts. The sand blasting can blow away the slightly bonded metal particles on the surfaces. The existing corrugations can be attributed to the stair stepping effect when building the curved or inclined struts by a layer-by-layer manufacruing mode in SLM, and will be diminished by decreasing the layer thickness, but this increases the time required to complete the fabrication.

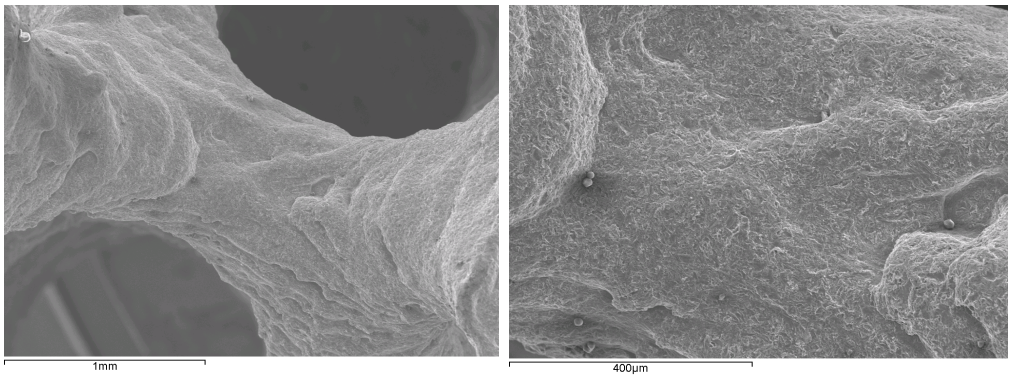

Figure 4 SEM images of strut surface of the Ti-6Al-4V TMPS cellular structures after the post processing

The SLM-built Gyroid TPMS cellular structures were compared to their designed CAD models to evaluate the manufacturing accuracy. The 3D micro-CT reconstructed models of the SLM-built Gyroid TPMS structures were superimposed on their 3D CAD models for both visual and quantifiable comparisons, as shown in Fig. 3. Fig. 3 (a) shows the Gyroid TPMS structure with 4mm cell size and 7.5% volume fraction. The gradient shows that the designed and built architectures nearly coincide at an average deviation of +0.1702/-0.1491 mm, indicating a very high accuracy of the SLM-built TPMS cellular structure. Similarly it can be seen in Fig. 3 (b) that the Gyroid structure with 7mm cell size and 7.5% volume fraction is very well reproduced in comparison to the original design CAD model with an average deviation of +0.1588/-0.1655 mm. The deviations may be attributed to the corrugations and roughness of the strut surfaces as shown in Fig. 4.

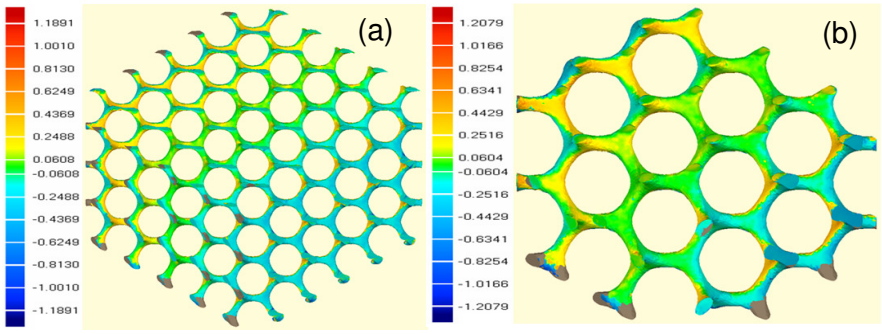

Figure 5 Comparisons of the 3D micro-CT reconstructed and 3D CAD models of the Gyroid TPMS cellular structures with a fixed volume fraction of 7.5% and the unit cell sizes of (a) 4mm and (b) 7mm

3.2 Microstructure of struts

Fig. 6 shows the microstructure of the struts of as-built Ti-6Al-4V TPMS structures with the optical, SEM and TEM micrographs. The optical micrograph in Fig. 6(a) reveals that the microstructure of the as-built struts exhibits the columnar grains filled with very fine and orthogonally oriented martensitic laths originating from the columnar grain boundaries. The fine martensitic laths can be interpreted as metastable hexagonal α' martensite (Yadroitsev et al. 2014; Sallica-Leva et al., 2013), and the columnar gain boundaries represent the prior β grains created upon solidification (Rafi et al. 2013). Microstructure evolution is primarily a function of cooling rate. Typically, upon a low cooling rate in the processing of Ti-6Al-4V, β phase transforms to α phase at a temperature of about 875 ^{o}C. But, it has been found that Ti-6Al-4V samples have entirely martensitic α' phase when exposed to cooling rates higher than 525 K/s (Ahmed and Rack, 1998). In the SLM process, the materials processed undergo a very high cooling rate with the order of 10^6 K/s (Thijs et al. 2010). Owing to such a high cooling rate experienced in SLM, β phase is completely transformed to fine α' martensite rather than α phase. The SEM micrograph in Fig. 6(b) demonstrates the near fully dense struts of the as-built Ti-6Al-4V TPMS structures. The TEM bright field image in Figure 6(c) reveals that the α' martensite appears long and narrow laths with the width ranging of 100~300 nm, which are aligned to one another. The inset of corresponding selected area electron diffraction (SAED) pattern in Figure 6(c) confirms that the α' martensitic laths possess the hexagonal close-packed crystal structure, and there is no α''' martensitic phase, which

has orthorhombic lattice structure (Simonelli 2014), in the examined area. The TEM micrograph with high magnification in Figure 6(d) shows a high dislocation density and many crystallographic defects (either stacking or twin faults) inside the α' martensitic grains, indicating that strain relaxation during the β → α' transformation is primarily accomplished by dislocation formation (Ahmed and Rack 1998). The previous literature revealed that the microhardness of as-built SLM Ti-6Al-4V varies with the processing parameters (Thijs et al. 2010), and is normally in the range of 3.43-4.90 GPa (Yadroitsev et al. 2014). The microhardness of the struts of as-made Ti-6Al-4V TPMS structures was measured to be 4.01±0.34 GPa, thus consistent with the hardness values reported in the other investigations (Thijs et al. 2010; Yadroitsev et al. 2014).

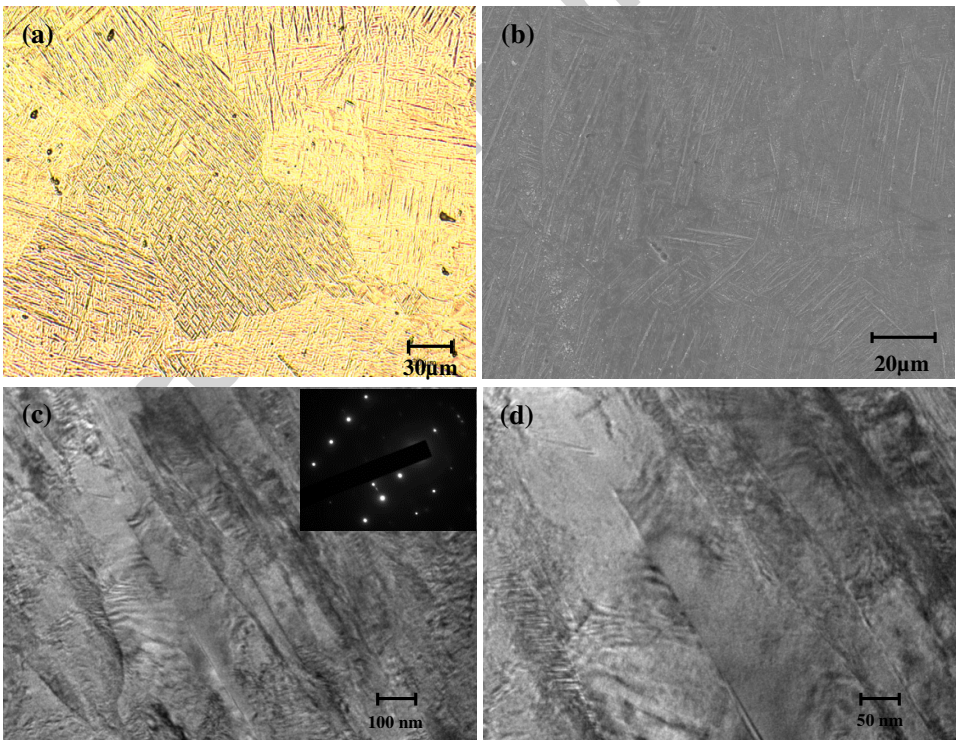

Fig. 6 Microstructure of the struts in as-built Ti-6Al-4V TPMS structures: (a) optical and (b) SEM micrographs, (c) TEM bright field image with the inset of corresponding

selected area diffraction pattern and (d) high magnification TEM micrograph showing dislocations and crystallographic defects (either stacking or twin faults) in the α' martensite grains

According to the requirement for implants materials specified in ISO 20160, a homogeneous microstructure of high-density biomaterials is necessary to provide material integrity and stability (Yadroitsev et al. 2014). Proper heat treatments are the normal way to control microstructure and mechanical properties of the Ti-6Al-4V alloy. In this work, the as-built samples were heat treated at 680 ^{o}C for 4 h and then cooled down in the furnace to RT in an argon atmosphere for thermal stress-relieving and microstructure homogenization. Fig. 7 depicts the microstructure of the heat-treated Ti-6Al-4V TPMS structures. From the optical and SEM micrographs in Figure 7(a) and (b) respectively, it can be observed that the heat treatment did not alter the morphologies of the prior β grains, which still remain visible, because the heat treatment temperature of 680 ^{o}C is much lower than the β-transus temperature of Ti-6Al-4V, about 1010^{o}C (Seshacharyulu et al. 2000). However, the heat treatment followed by slow furnace cooling have a significantly influence on the phase composition and morphologies. The TEM bright field image in Figure 7(c) shows that the fine α' martensitic structure has been transformed to a mixture of α and β, in which the α phase being the dominant fraction is present as fine laths and separated by narrow, interphase regions of dark β phase. The width of the α grains was measured to be in the range of 500-800 nm, obviously bigger than that of the α' martensitic laths retained in the as-built samples as shown in Figure 6. It is possible that the heat treatment temperature of 680^{o}C, which is above the martensite start temperature (M_s) for Ti-6Al-4V alloy at around 650 ^{o}C (Elmer et al. 2004), and slow furnace cooling enable the phase transformation of α'→ α + β. The high magnification TEM

micrograph in Figure 7(d) demonstrates that the α phase in the heat-treated Ti-6Al-4V possesses a lower dislocation density and less crystallographic defects compared to the α' martensite in the as-built Ti-6Al-4V. Selected area diffraction analysis further confirmed that the α phase has a hexagonal crystal structure, identical to that of the acicular α' martensite observed in the as-built samples. The microhardness of the struts of the heat-treated Ti-6Al-4V TPMS structures is 3.71±0.35 GPa, lower than that of the as-built TPMS structures. The decrease in microhardness after heat treatment is expected due to the coarsening of the microstructure compared to the original finer α' martensites. The previous works also observed the decrease in the yield stress, ultimate tensile strength and microhardness of SLM-produced Ti-6Al-4V after heat treatment (Vranchen et al., 2012; Yadroitsev et al. 2014).

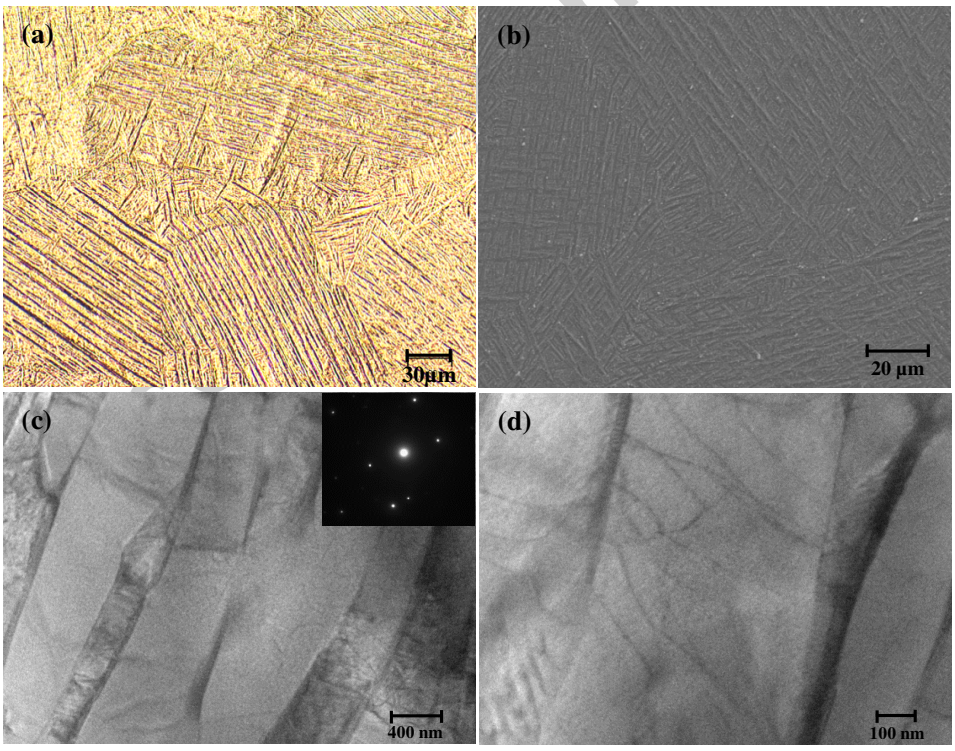

Fig. 7 Microstructure of the struts in heat-treated Ti-6Al-4V TPMS structures: (a) optical and (b) SEM micrographs, (c) TEM bright field image with the inset of

corresponding selected area diffraction pattern and (d) high magnification TEM micrograph showing dislocations

Fig. 8(a) and (b) depict the XRD patterns of the struts in the Ti-6Al-4V TPMS cellular structures before and after the heat treatment, respectively. In the both XRD patterns, only peaks corresponding to the hexagonal close-packed titanium (hcp-Ti) are observed, indicating that α and α' have the same crystal structure. But, the diffraction peaks of the as-built sample in Fig. 8(a) are broad owing to the high crystal distortion of α' phase, while the diffraction peaks after the heat treatment in Fig. 8(b) become much narrower and sharper, indicating the presence of α phase, which is an equilibrium phase and has a lower crystal distortion compared to the α' phase (Sallica-Leva et al., 2013). Additionally, the peak intensities in the as-built condition are significantly lower than those of the heat-treated sample, indicating finer microstructure in this case. The absence of peaks corresponding to the β phase in the heat treated sample may be due to the very small β phase fraction caused by the heat treatment temperature of 680^{o}C, which is much lower compared to the β-transus temperature of Ti-6Al-4V, as the β phase fraction is increasing with increasing heat treatment temperature (Leuders et al. 2013).

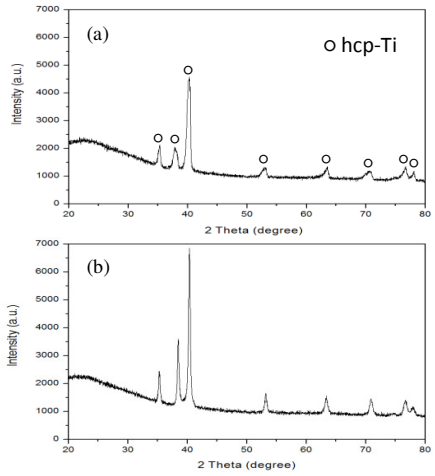

Fig. 8 XRD patterns of the struts in SLM-produced Ti-6Al-4V TPMS structures (a) before and (b) after heat treatment

3.3 Densities of the struts

The densities of the struts have an important effect on the properties, especially mechanical properties of porous materials. Achievement of near fully dense struts is normally expected in the SLM process in order to obtain strong and high-performance lattice structures. Table 1 lists the relative densities of the struts of the Gyroid and Diamond TPMS lattices with different porosities manufactured in this work. It can be found that high relative densities (above 99%) of the struts can be achieved for the Gyroid and Diamond Ti-6Al-4V TPMS lattices with the porosities ranging of 80-95%. These TPMS lattices were built using the optimized processing parameters, which were proposed by the SLM machine provider for the Ti-6Al-4V powder. It seems that the porosity of Ti-6Al-4V TPMS lattices has little effect on the strut densities. It is noted that the processing parameters and scan strategy in the SLM process play a crucial role in making high density parts (Kruth et al., 1999), and therefore it is worth carefully investigating the effects of the SLM processing parameters and scan strategy on the strut density of TPMS lattices in the future works.

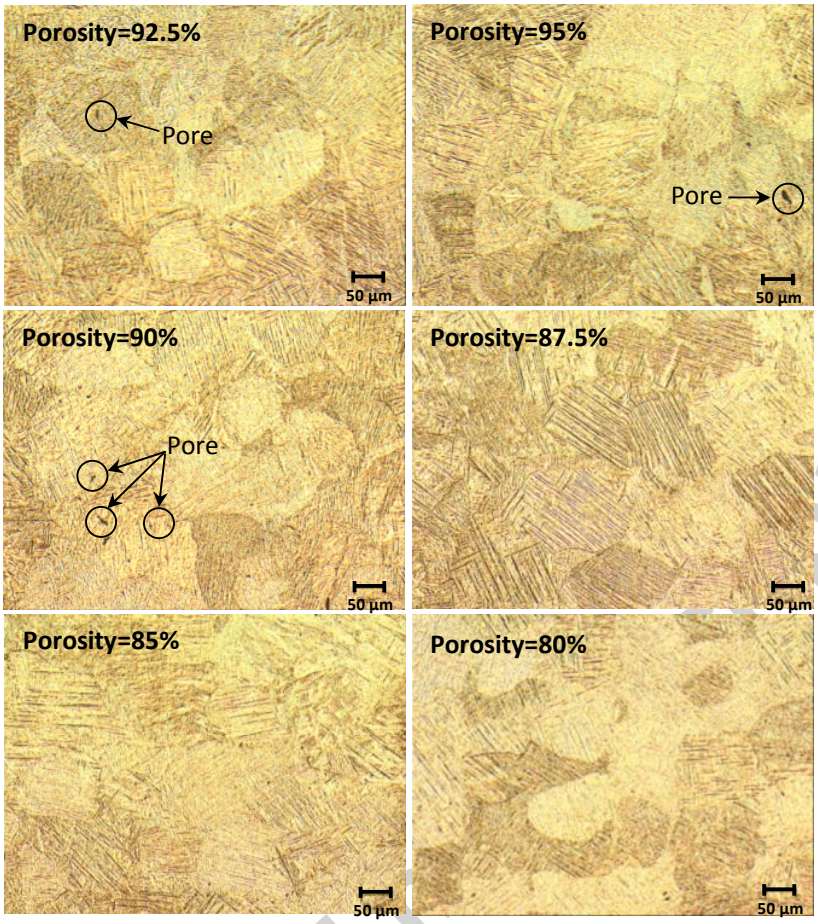

Fig. 9 Optical micrographs of the strut cross sections of Ti-6Al-4V Diamond TMPS lattices with the same unit cell size of 5mm and different porosities

Fig. 9 shows the optical micrographs of the strut cross sections of the Ti-6Al-4V Diamond TMPS lattices with different porosities. The SEM and optical micrographs in Fig. 6, 7 and 9 all demonstrates the near fully dense struts of the as-built Ti-6Al-4V TPMS structures, which is consistent with the density measurements. But a very small amount of spherical or irregular pores and micro cracks with the small dimensions ranging of 1-20 µm is still observable. This small amount of defects like micro pores and cracks may be attributed to the high residual stress, gas entrapment and keyhole effect caused by metal evaporation in the laser scanning (Gong 2013; Attar et al., 2014).

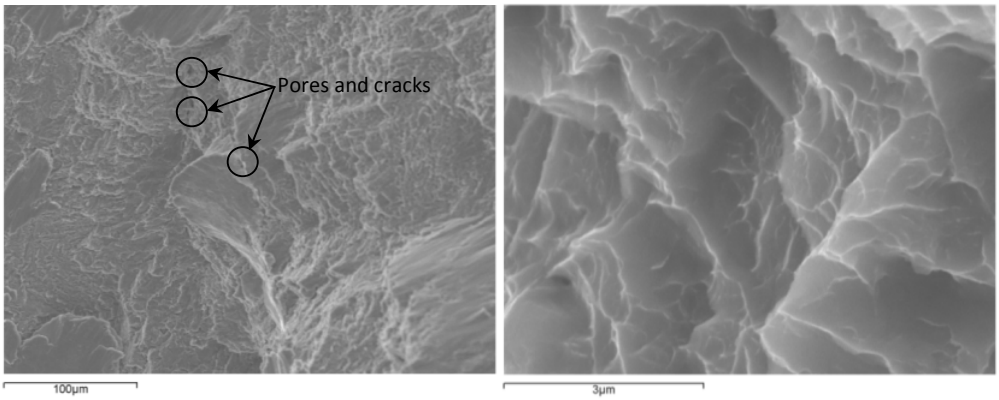

Fig. 10 SEM micrographs of the typical fractured surface of Ti-6Al-4V TMPS lattice struts after the compression testing at increasing magnifications

Fig. 10 shows the SEM micrographs of the typical fractured surface of Ti-6Al-4V TMPS lattice struts after the compression testing. From the SEM micrographs in Fig. 10, solid material with only a few small pores and cracks on the strut fractured surfaces can be observed, which further confirms that Ti-6Al-4V TPMS lattices with near fully dense struts can be built in the SLM process.

3.4 Mechanical properties

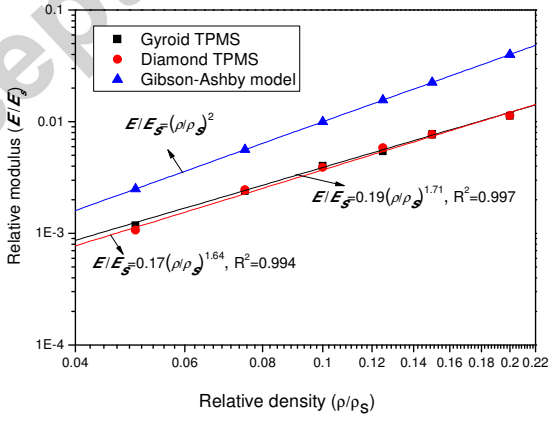

(a)

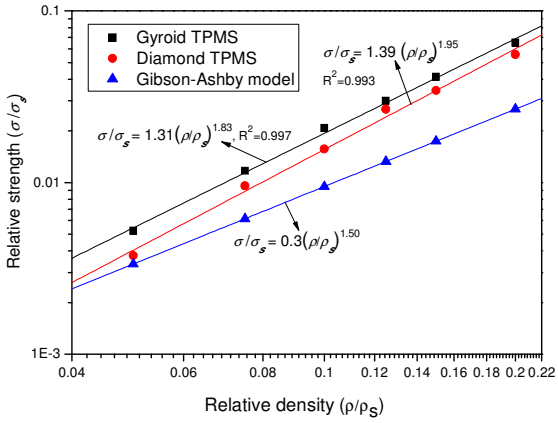

(b)

Fig.11 Variation of (a) the relative modulus and (b) relative strength of the Ti-6Al-4V TPMS lattices with relative density

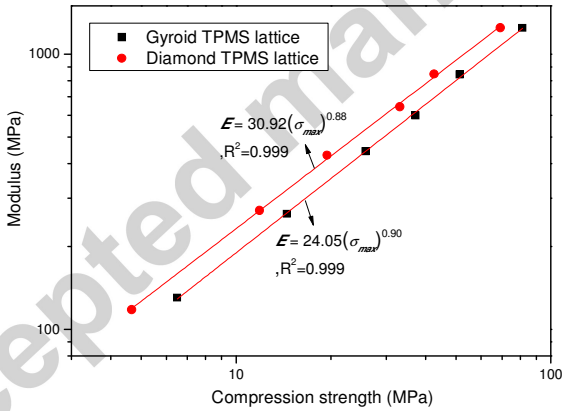

Fig.12 Elastic modulus as a function of the ultimate compression strength for the Ti-6Al-4V TPMS lattices

Generally, the mechanical properties of cellular structures are governed by the relative density, the cell architecture and cell anisotropy (Heinl et al. 2008). Gibson and Ashby provide simple relations between the elastic modulus and relative density, and yield strength and relative density for open-celled structures with randomly distributed porosity and perfectly smooth surfaces (Gibson and Ashby, 2007):

$$\frac{E}{E_s} = (\frac{\rho}{\rho_s})^2 \quad (1)$$

$$\frac{\sigma}{\sigma_s} = 0.3 \times (\frac{\rho}{\rho_s})^{1.5} \quad (2)$$

Where E_s, ρ_s and σ_s are the elastic modulus, density and yield strength of fully dense solid materials, and E, ρ and σ are the apparent modulus, density and yield strength of open-cell cellular structures. E_s was assumed to be 110GPa for fully dense Ti-6Al-4V (Harrysson et al., 2008). $\sigma_{y,s}$ for many metals and alloys is roughly a third of the Vickers microhardness (Murr et al., 2010). In this work, the Vickers microhardness of the struts is 3.71±0.35 GPa, and thus $\sigma_{y,s}$ was taken as 1.24 GPa.

Fig. 11(a) shows log-log plots of the relative modulus versus relative density values. The Gyroid and Diamond TPMS lattice data points were well fitted to the straight lines with the coefficients of determination (R^2) of 0.997 and 0.993, respectively. Fig. 11(b) shows log-log plots of the relative strength versus relative density values. Also, there exist straight-line fits for the relative strength-relative density data points of Gyroid and Diamond TPMS lattices with the R^2 of 0.997 and 0.994, respectively. Therefore, the mechanical properties of the Ti-6Al-4V TPMS lattices correlate well with the relative density (R^2>0.99), and the equations indicating the explicit correlations between the modulus and compression strength of the SLM-made Ti-6Al-4V TPMS lattices and relative density like the Gibson-Ashby model are derived as shown in Fig. 11. Owing to the exactly established correlations between the mechanical properties and relative density, it is possible to precisely predict and even design the mechanical properties of the Ti-6Al-4V TPMS lattices by adjusting the volume fraction. The correlations between the modulus and compression strength fitted in Fig. 12 indicate that the modulus and strength vary dependently for a given structural design.

As shown in Fig. 11, the determined exponents and scaling factors for the correlations of the characteristic value with the relative density differ from the exponents and scaling factors predicted by the Gibson-Ashby model. These differences might be explained by the following three reasons. The first explanation relates to the inherent residual stress, which induces early strut failure by plastic yielding, and then results in lower mechanical properties (Van Bael et al., 2011). The second explanation is that the irregular struts with the existing corrugations as shown in Fig. 4 differ from the assumptions of straight beams and perfectly smooth surfaces in the Gibson-Ashby model. The last explanation is that the TPMS lattice structures in this work belong to non-stochastic periodic structures, which are different from the open-celled structures with randomly distributed porosity in the Gibson-Ashy model.

Table 2 shows a comparison in the mechanical properties and porosities of the Ti-6Al-4V TPMS lattice structures and human bone. In Table 2, the mechanical properties of the 80-95% porosity TPMS lattices were experimentally measured, whereas those of the 5-10 porosity lattices were predicted through the fitted correlations shown in Fig. 11. It should be noted that the mechanical properties of human bone vary depending on anatomical site, age, loading direction and sex. Consequently, the listed values of trabecular and cortical bone in Table 2 should only represent the dimensions of bone's properties. The 80-95% porosity TPMS lattices exhibit a comparable porosity with trabecular bone, and the modulus can be adjusted to the modulus of trabecular bone. At the same range of porosity of 5-10%, the moduli of cortical bone and of the Ti-6Al-4V TPMS lattices are in a similar range. Therefore, the moduli and porosities of the Ti-6Al-4V TPMS lattices can be simultaneously tailored to the levels of human bones and thus reduce or avoid "stress

shielding" and increase longevity of implants. This is a very important result with respect to the application of the Ti-6Al-4V TPMS lattice structures built by SLM as biomaterials for bone replacement. Furthermore, the compression strength of the TPMS lattice structures is superior to the compression strength of human bone at equal values of modulus.

Moreover, both the SLM-manufactured Gyroid and Diamond TPMS lattices have an interconnected high porosity of 80-95% and the pore sizes ranging of 560-1600 μm and 480-1450 μm, respectively. Otsuki et al. (2006) revealed that the pores of porous bioactive titanium implants should be interconnected in order to ensure the bone ingrowth. They evaluated porous implants with two levels of porosity (50% and 70%) and two ranges of pore sizes (250 - 500 μm and 500 – 1500 μm) and concluded that the pore size ranging from 500 to 1500 μm for both levels of porosity obtain a tissue of good quality. Therefore, the high interconnected porosity with appropriate pore sizes in the SLM-made Ti-6Al-4V TPMS lattices can provide biological anchorage via the ingrowth of mineralized tissue into the pore space, resulting in a good and permanent fixation of the implant in the surrounding bone tissue.

Conclusions

In this work, Ti-6Al-4V Gyroid and Diamond triply periodic minimal surface (TPMS) lattice structures were manufactured by selective laser melting (SLM) for bone implants. The manufacturability, microstructure and mechanical properties of SLM-made Ti-6Al-4V TPMS lattices were evaluated.

(1) Plenty of raw metal particles are bonded on the strut surfaces of the as-built Ti-6Al-4V TMPS lattices, but nearly all of them can be removed by a post processing of heat treatment followed by sand blasting.

(2) Visual and quantifiable comparisons by superimposing 3D micro-CT reconstructed models of the Ti-6Al-4V TPMS lattices on their 3D CAD models shows excellent reproduction of the designs.

(3) The as-built Ti-6Al-4V struts exhibit the microstructure of columnar grains filled with very fine and orthogonally oriented α' martensitic laths with the width of 100~300 nm and have the microhardness of 4.01±0.34 GPa. After heat treatment at 680 ^{o}C for 4 h, the α' martensite was converted to a mixture of α and β, in which the α phase being the dominant fraction is present as fine laths with the width of 500-800 nm and separated by a small amount of narrow, interphase regions of dark β phase. Also, the microhardness is decreased to 3.71±0.35 GPa owing to the coarsening of the microstructure.

(4) Mechanical properties of the TPMS lattices correlate well with their relative density, and the equations indicating the explicit correlations between the modulus and compression strength, and relative density were derived. Therefore, it is possible to precisely predict and even design the mechanical properties of the SLM-made Ti-6Al-4V TPMS lattices.

(5) The 80-95% porosity TPMS lattices exhibit a comparable porosity with trabecular bone, and the modulus is in the range of 0.12-1.25 GPa and thus can be adjusted to the modulus of trabecular bone. At the same range of porosity of 5-10%, the moduli of cortical bone and of the Ti-6Al-4V TPMS lattices are in a similar range. Therefore, the modulus and porosity of the Ti-6Al-4V TPMS lattices can be tailored to the levels

of human bones and thus reduce or avoid “stress shielding” and increase longevity of implants.

In conclusion, due to the biomorphic designs, and high interconnected porosity with appropriate pore sizes and stiffness comparable to human bones, the Ti-6Al-4V TPMS lattices made by SLM can be a promising material for load bearing bone implants.

Acknowledgement

This work is supported by the UK Technology Strategy Board (TSB) funded project (TP14/BA036D) entitled “SAVING - Sustainable product development via design optimisation and AdditiVe manufacturing”, National Natural Science Foundations of China (Grant no. 51375188 and 51375189) and the Guangdong Innovative and Entrepreneurial Research Team Program (NO.2013C071). The authors would like to thank Dr Simon Lawrence Bubb in 3T RPD Ltd for manufacturing the samples and Dr Hong Chang, Dr Yat-Tarng Shyng and Dr Wear Lesley in University of Exeter for the assistance with the measurements of optical microscope, SEM, TEM and mechanical properties.

References

Ahmed, T., Rack, H.J., 1998. Phase transformations during cooling in α + β titanium alloys. Mat. Sci. Eng. A-Struct., 243(1-2), 206-211.

Attar, H., Bönisch, M., Calin, M., Zhang, L.C., Scudino, S., Eckert, J., 2014. Selective laser melting of in situ titanium–titanium boride composites: Processing, microstructure and mechanical properties. Acta Mater., 76, 13-22.

Bertol, L.S., Júnior, W.K., da Silva, F.P., Aumund-Kopp, C., 2010. Medical design: Direct metal laser sintering of Ti–6Al–4V. Mater. Design, 31, 3982-3988.

Brandl, E., Michailov, V., Viehweger, B., Leyens, C., 2011. Deposition of Ti–6Al–4V using laser and wire, part I: Microstructural properties of single beads. Surf. Coat. Tech., 206(6), 1120-1129.

Curodeau, A., Sachs, E., Caldarise, S., 2000. Design and Fabrication of Cast Orthopedic Implants with Freeform Surface Textures from 3-D Printed Ceramic Shell. J. Biomed. Mater. Res. A, 53(5), 525-535.

Davis, N.G., Teisen, J., Schuh, C., Dunand, D.C., 2001. Solid-state foaming of titanium by superplastic expansion of argon-filled pores. J. Mater. Res., 16, 1508–1539.

Elmer, J.W., Palmer, T.A., Babu, S.S., Zhang, W., DebRoy, T., 2004. Phase transformation dynamics during welding of Ti-6Al-4V. J. Appl. Phys., 95(12), 8327-8339.

Fujibayashi, S., Neo, M., Kim, H.M., Kokubo, T., Nakamura, T., 2004. Osteoinduction of porous bioactive titanium metal. Biomaterials, 25(3), 443-450.

Galanete, J., Rostoker, W., 1973. Fiber Metal Composites in the Fixation of Skeleta1 Prosthesis. J. Biomed. Mater. Res. A, 4, 43-61.

Gibson, L.J., Ashby, M.F., 1997. Cellular Solids: Structure and Properties, Cambridge University Press, New York.

Gong, H., 2013. Generation and detection of defects in metallic parts fabricated by selective laser melting and electron beam melting and their effects on mechanical properties. Department of Industrial Engineering Louisville, Kentucky, University of Louisville. PhD thesis.

Gorny, B., Niendorf, T., Lackmann, J., Thoene, M., Troester, T., Maier, H. J., 2011. In situ characterization of the deformation and failure behavior of non-stochastic porous

structures processed by selective laser melting. Mat. Sci. Eng. A-Struct., 528(27), 7962-7967.

Hrabe, N.W., Heinl, P., Flinn, B., Korner, C., Bordia, R.K., 2011. Compression-compression fatigue of selective electron beam melted cellular titanium (Ti-6Al-4V). J. Biomed. Mater. Res. B, 99B, 313–320.

Heinl, P., Muller, L., Korner, C., Singer, R. F., Muller, F. A., 2008. Cellular Ti-6Al-4V structures with interconnected macro porosity for bone implants fabricated by selective electron beam melting. Acta Biomater., 4(5), 1536-1544.

Huiskes, R., Weinans, H., van Rietbergen, B., 1992. The relationship between stress shielding and bone resorption around total hip stems and the effects of flexible materials. Clin. Orthop. Relat. R., 274, 124-134.

Koike, M., Greer, P., Owen, K., Lilly, G., Murr, L.E., Gaytan, S.M., Martinez, E., Okabe, T., 2011. Evaluation of Titanium Alloys Fabricated Using Rapid Prototyping Technologies-Electron Beam Melting and Laser Beam Melting. Materials, 4(12), 1776-1792.

Kruth, J. P., Kumar, S., Van Vaerenbergh, J., 2005. Study of laser-sinterability of ferro-based powders. Rapid Prototyping J., 11(5), 287-292.

Leuders, S., Thöne, M., Riemer, A., Niendorf, T., Tröster, T., Richard, H.A., Maier, H.J., 2013. On the mechanical behaviour of titanium alloy TiAl6V4 manufactured by selective laser melting: Fatigue resistance and crack growth performance. Int. J. Fatigue, 48, 300-307.

Li, J.P., Li, S.H., Van Blitterswijk, C.A., de Groot, K., 2005. A novel porous Ti6Al4V: characterization and cell attachment. J. Biomed. Mater. Res. A, 73(2), 223-233.

Li, J.P., de Wijn, J.R., Van Blitterswijk, C.A., de Groot, K., 2006. Porous Ti6Al4V scaffold directly fabricating by rapid prototyping: preparation and in vitro experiment. Biomaterials, 27(8), 1223-1235.

Melchels, F.P., Bertoldi, K., Gabbrielli, R., Velders, A.H., Feijen, J., Grijpma, D.W., 2010a. Mathematically defined tissue engineering scaffold architectures prepared by stereolithography. Biomaterials, 31(27), 6909-6916.

Melchels, F.P., Barradas, A.M., van Blitterswijk, C.A., de Boer, J., Feijen, J., Grijpma, D.W., 2010b. Effects of the architecture of tissue engineering scaffolds on cell seeding and culturing. Acta Biomater., 6(11), 4208-4217.

Murr, L. E., Gaytan, S.M., Medina, F., Martinez, E., Martinez, J.L., Hernandez, D.H., Machado, B.I., Ramirez, D.A., Wicker, R.B., 2010. Characterization of Ti–6Al–4V open cellular foams fabricated by additive manufacturing using electron beam melting. Mat. Sci. Eng. A-Struct., 527(7-8), 1861-1868.

Mullen, L., Stamp, R.C., Brooks, W.K., Jones, E., Sutcliffe, C.J., Biomed, J., 2009. Selective laser melting: a regular unit cell approach for the manufacture of porous, titanium, bone in-growth constructs, suitable for orthopedic applications, J. Biomed. Mater. Res. B, 89B, 325-334.

Oh, I.K., Nomura, N., Hanada, S., 2003. Mechanical properties of porous titanium compacts prepared by powder sintering. Scripta Mater., 49,1197–202.

Pattanayak, D. K., Fukuda, A., Matsushita, T., Takemoto, M., Fujibayashi, S., Sasaki, K., Nishida, N., Nakamura, T., Kokubo, T., 2011. Bioactive Ti metal analogous to human cancellous bone: Fabrication by selective laser melting and chemical treatments. Acta Biomater. 7, 1398-1406.

Parthasarathy, J., Starly, B., Raman, S., Christensen, A., 2010. Mechanical evaluation of porous titanium (Ti6Al4V) structures with electron beam melting (EBM). J. Mech. Behav. Biomed. 3(3), 249-259.

Rajagopalan, S., Robb, R.A., 2006. Schwarz meets Schwann: design and fabrication of biomorphic and durataxic tissue engineering scaffolds. Med. Image. Anal., 10(5), 693-712.

Rafi, H. K., Karthik, N.V., Gong, H., Starr, T.L., Stucker, B.E., 2013. A comparison of the tensile, fatigue, and fracture behavior of Ti–6Al–4V and 15-5 PH stainless steel parts made by selective laser melting. Int. J. Adv. Manuf. Tech., 69(5-8), 1299-1309.

Reilly, D.T., Burstein, A.H., 1975. The elastic and ultimate properties of compact bone tissue. J. Biomech., 8, 393–405.

Sallica-Leva, E., Jardini, A.L., Fogagnolo, J.B., 2013. Microstructure and mechanical behavior of porous Ti-6Al-4V parts obtained by selective laser melting. J. Mech. Behav. Biomed., 26, 98-108.

Seshacharyulu, T., Medeiros, S.C., Frazier, W.G., Prasad, Y.V.R.K., 2000. Hot working of commercial Ti–6Al–4V with an equiaxed α–β microstructure: materials modeling considerations. Mat. Sci. Eng. A-Struct., 284, 184-194.

Sevilla P., Aparicio C., Planell J.A., Gil F.J., 2007. Comparison of the mechanical properties between tantalum and nickel-titanium foamsimplant materials for bone ingrowth applications. J Alloy. Comp., 439, 67–73.

Schoen, A.H., 1970. Infinite periodic minimal surfaces without self-intersections. NASA Technical report TN D-5541, Washington, DC.

Schwarz, H., 1885. Gesammelte Mathematische Abhandlungen, vols. 1&2. Springer, Berlin.

Sikavitsas, V.I., Temenoff, J.S., Mikos, A.G., 2001. Biomaterials and bone mechanotransduction, Biomaterials, 22, 2581-2593.

Simonelli, M., 2014. Microstructure evolution and mechanical properties of selective laser melted Ti-6Al-4V. School of Aeronautical, Automotive, Chemical and Materials Engineering, Department of Materials, Loughborough University. PhD thesis.

Spalazzi, J.P., Dionisio, K.L., Jiang, J., Lu, K.K., 2003. Osteoblast and Chondrocyte interactions during coculture on scaffolds. IEEE Eng. Med. Biol., 22 (5), 27–34.

Thijs, L., Verhaeghe, F., Craeghs, T., Van Humbeeck, J., Kruth, J. P., 2010. A study of the micro structural evolution during selective laser melting of Ti-6Al-4V. Acta Biomater., 58(9), 3303-3312.

van Blitterswijk, C.A., Ktijp, W., Daems, W.Th., de Groot, K., 1986. Macropore tissue ingrowth: quantitative and qualitative hydroxyapatite ceramic. Biomaterials, 7, 137-143.

Yan, C. Z., Hao, L., Hussein, A., Raymont, D., 2012. Evaluations of cellular lattice structures manufactured using selective laser melting. Int. J. Mach. Tool. Manu., 62, 32-38.

Yousaf, M.N., Houseman, B.T., Mrkisch, M., 2001. Using electroactive substrates to pattern the attachment of two different cell populations. PNAS, 98(11), 5992–5996.

Van Bael, S., Kerckhofs, G., Moesen, M., Pyka, G., Schrooten, J., Kruth, J.P., 2011. Micro-CT-based improvement of geometrical and mechanical controllability of selective laser melted Ti6Al4V porous structures. Mat. Sci. Eng. A-Struct., 528(24), 7423-7431.

Otsuki, B., Takemoto, M., Fujibayashi, S., Neo, M., Kokubo, T., Nakamura, T., 2006. Pore throat size and connectivity determine bone and tissue ingrowth into porous implants: three-dimensional micro-CT based structural analyses of porous bioactive titanium implants. Biomaterials, 27, 5892–5900.

Vrancken, B., Thijs, L., Van Humbeeck, J., Kruth, J. P. (2012). "Heat treatment of Ti6Al4V produced by Selective Laser Melting: Microstructure and mechanical properties." Journal of Alloys and Compounds 541: 177-185.

Figure captions

Figure 1 SEM images of the Ti-6Al-4V powder with different magnifications

Figure 2 CAD models of the unit cells and TMPS cellular structures, and optical micrographs of as-built Ti-6Al-4V TMPS cellular structures

Figure 3 SEM images of strut surface of the as-built Ti-6Al-4V TMPS cellular structures without post processing

Figure 4 SEM images of strut surface of the Ti-6Al-4V TMPS cellular structures after the post processing

Figure 5 Comparisons of the 3D micro-CT reconstructed and 3D CAD models of the Gyroid TPMS cellular structures with a fixed volume fraction of 7.5% and the unit cell sizes of (a) 4mm and (b) 7mm

Fig. 6 Microstructure of the struts in as-built Ti-6Al-4V TPMS structures: (a) optical and (b) SEM micrographs, (c) TEM bright field image with the inset of corresponding selected area diffraction pattern and (d) high magnification TEM micrograph showing dislocations and crystallographic defects (either stacking or twin faults) in the α' martensite grains

Fig. 7 Microstructure of the struts in heat-treated Ti-6Al-4V TPMS structures: (a) optical and (b) SEM micrographs, (c) TEM bright field image with the inset of corresponding selected area diffraction pattern and (d) high magnification TEM micrograph showing dislocations

Fig. 8 XRD patterns of the struts in SLM-produced Ti-6Al-4V TPMS structures (a) before and (b) after heat treatment

Fig. 9 Optical micrographs of the strut cross sections of Ti-6Al-4V Diamond TMPS lattices with the same unit cell size of 5mm and different porosities

Fig. 10 SEM micrographs of the fractured surface of Ti-6Al-4V TMPS lattice struts after the compression testing at increasing magnifications

Fig.11 Variation of (a) the relative modulus and (b) relative strength of the Ti-6Al-4V TPMS lattices with relative density

Fig.12 Elastic modulus as a function of the ultimate compression strength for the Ti-6Al-4V TPMS lattices

Table 1 Relative densities of the struts of the Gyroid and Diamond TPMS lattices with the same unit cell size of 5mm and different porosities

Porosity (%)	Relative density (%)	
	Gyroid TPMS	Diamond TPMS
95	99.2±0.3	99.4±0.4
92.5	99.4±0.2	99.2±0.3
90	99.3±0.3	99.2±0.2
87.5	99.5±0.3	99.5±0.2
85	99.5±0.2	99.6±0.3
80	99.4±0.3	99.3±0.3

Table 2 Comparison in mechanical properties and porosity between the Ti-6Al-4V TPMS lattice structures and human bone

Materials	Porosity (1-volume fraction, %)	Pore size (μm)	Elastic modulus (GPa)	Compression strength (MPa)
Gyroid TPMS lattices	80-95	560-1600	0.13±0.02～1.25±0.04	6.50±1.62～81.30±2.60
	5-10	-	17.45～19.14 [a]	1342～1481 [a]
Diamond TPMS lattices	80-95	480-1450	0.12±0.03～1.25±0.07	4.66±2.13～69.21±4.22
	5-10	-	15.73～17.19 [a]	1403～1559 [a]
Trabecular bone	50-90 [b]	-	1.08±8.0 [c]	25.0±8.1 [c]
Cortical bone	5-10 [b]	-	18.2±0.85 [d]	205±12.6 [d]

[a] Predicted by the equations shown in Fig. 9
[b] Ref. (Sikavitsas et al., 2001)
[c] Ref. (Sevilla et al., 2007)
[d] Ref. (Heinl et al., 2008)

1. Ti-6Al-4V triply periodic minimal surface lattices are made by selective laser melting.

2. Characterisation of the lattices shows excellent reproduction of the designs.

3. Modulus and porosity of the lattices can be tailored to the levels of human bones.